Research Paper

A New Relaying Method for Protecting Shunt Compensated Transmission Line Integrated with DFIG Wind Farm

Omkar Koduri [1, *], *R. Ramachandran* [1] (ID) , and *M. Saiveerraju* [2]

[1]*Department of Electrical Engineering, Faculty of Engineering and Technology, Annamalai University, Annamalainagar, 608002, Chidambaram, Tamil Nadu, India.*
[2]*Department of Electrical and Electronics Engineering, Sagi Rama Krishnam Raju Engineering College, Bhimavaram, 534202, A.P, India.*

Abstract— The distance relays on transmission lines connecting Doubly Fed Induction Generator (DFIG) wind farms with a Static Synchronous Compensator (STATCOM) face challenges in ensuring reliable protection due to the system unique fault characteristics and varying operating modes. This work presents a new relaying method that integrates Particle Swarm Optimization (PSO) with Variational Mode Decomposition (VMD) and Dominant Mode Filtering-Teager-Kaiser Energy Operator (DMF-TKEO) for fault detection. For fault classification, it employs a combination of PSO-VMD and a Modified Jellyfish Optimization-tuned Random Vector Functional Link (MJO-RVFL) network. The fault detection technique focuses on optimizing the parameters (α and K) of the existing variational mode decomposition by minimizing the mean envelope entropy. The optimal Intrinsic Mode Functions (IMFs) are then derived, from which the dominant mode is identified using the Pearson correlation and fault detection is accomplished through the Teager-Kaiser energy operator. In the proposed fault classification framework, the grid-side currents are decomposed using the particle swarm optimization-based variational mode decomposition. The resulting optimal IMFs are employed to identify the most appropriate IMF, which is subsequently used to extract energy features. These features are then provided as input to MJO-RVFL network for fault classification. To assess the effectiveness of the proposed protection scheme, different fault and non-fault scenarios are created on a two-bus test power system through MATLAB/Simulink. The results demonstrate the effectiveness of the proposed protection scheme, confirming its suitability for securing such critical transmission lines. The proposed method gives 100% fault detection accuracy and 99.97% accuracy for fault classification. Furthermore, the proposed classifier achieves the performance metrics like Precision (0.995), Recall (0.992) and F1-Score (0.994), providing quantitative insights into its accuracy and dependability Finally, a proposed algorithm is compared with similar works in literature.

Keywords—Distance protection, doubly fed induction generator, static synchronous compensator, variational mode decomposition, particle swarm optimization, modified jellyfish optimization, random vector functional link network.

NOMENCLATURE

α	Penalty factor
β	Distribution coefficient
$\hat{X}$	Desired output
Ω	Resistance
$\Psi[x_c(n)]$	Energy
$C(t)$	Time control function
C_1, C_2	Control the particle movement
D	Jellyfish current direction
E_A	Energy of Phase A
E_B	Energy of Phase B
E_C	Energy of Phase C
E_z	Energy of Zero Sequence current
I	Motion coefficient
I_{diff}	Differential current
K	Optimal number of modes
K_{max}	Number of iterations
K_{th}	Hidden node
L_b	Lower bound
Max_{iter}	Maximum iterations
N	Number of samples
N_{pop}	Number of populations
p_i	Normalized envelope
Q_1, Q_3	First and third quartiles
Q_{ref}	Reactive power reference
$r(x(n))$	Pearson correlation coefficient
r_1	Random number
U_b	Upper bound
u_k	Model function vector
V_{ref}	Reference voltage
X	Actual output
$X_d(n)$	Dominant mode signal
X_i	Jellyfish vector
Z_{app}	Apparent impedance
ε_T	Threshold
R_f	Fault resistance
CA	Classification Accuracy
DFIG	Doubly Fed Induction Generator
DMF	Dominant Mode Filtering

O. Koduri *et al.*: A New Relaying Method for Protecting Shunt Compensated Transmission Line Integrated with DFIG Wind Farm

2

FACTS   Flexible AC Transmission System
FCU   Fault Classification Unit
FDU   Fault Detection Unit
HHT   Hilbert-Huang Transform
IMFs   Intrinsic Mode Functions
JSO   Jellyfish Search Optimizer
kHz   Kilohertz
MEE   Minimum Mean Envelope
MEEE   Minimum Mean Envelope Entropy
MJO   Modified Jellyfish Optimization
MSE   Mean Square Error
p.u   Per unit
PSO   Particle Swarm Optimization
Rand   Random number
RG   Grid side relay
RVFL   Random Vector Functional Link Neural Network
Rw   Wind side relay
STATCOM Static Synchronous Compensator
TEKO   Teaser-Kaiser Energy Operator
VARCM   VAR Control Mode
VMD   Variational Mode Decomposition
VRM   Voltage Regulator Mode
WT   Wavelet Transform

1. INTRODUCTION

1.1. Motivation

To meet future crucial energy demands and goals, wind energy is going to become a more vital requirement [1]. Power electronics converters and sophisticated control and information technologies are essential components of large-scale renewable energy generation is presented in [2]. The development of DFIG wind farms that integrate to transmission line is reported in [3]. As wind capacity continues to grow, current grid regulations require that wind farms remain connected during system disturbances and supply reactive power to the grid. Hence, voltage stability and low-voltage ride-through capabilities are key for large-scale DFIG connected to the grid [4]. Compensating devices based on Flexible AC Transmission Line Systems (FACTS) have been used recently to encourage the integration of large-capacity wind farms into the grid is presented in [5]. The time-domain distance relay, which is appropriate for wind power integration systems, is based on the R-L differential-equation algorithm is presented in [6]. However, the variation of output power of DFIG win farm and control strategy are influence the conventional distance relay operation. The transient energy and time-time transform based fault detection and classification of DFIG-wind farm collector lines is presented in [7]. However, this scheme is not addressed the system configuration and wind power rating. The digital differential relay for fault detection and optimized support vector machine is presented in [8]. Nevertheless, it does not account for the impact of high fault resistance and noise condition on performance. A new hybrid machine learning classifier for protection of large scale DFIG wind farm is reported in [9]. However, the accuracy with different noise and high fault impedance cases are does not considered. The incorporation of converter-based renewable resources affects the performance of the existing line distance protection is presented in [10]. Conversely, it does not account for the impact of wind farm variation and system change. In [11], adaptive coeffient based distance relay algorithm is presented. Nevertheless, it does not address the impact of noise condition and wind farm capacity variation. The transient function for STATCOM control to improve high voltage ride through is presented in [12]. Nevertheless, it does not account for impact of wind farm capacity variations. This paper primarily aims to examine the functioning of distance relays and develop an improved protection scheme for transmission lines with STATCOM compensation that connect to DFIG wind farms.

1.2. Literature review

A pilot protection approach based on Spearman rank correlation coefficient.is presented in [13]. However, this method does not validate the effect of noise and CT saturation condition. In [14] it introduces an adaptive protection scheme based on the phase relationship of fault and measured current. However, this scheme has poor selectivity due to the weak infeed characteristics of wind farms. Taylor series index based fault detection for DFIG integrated STATCOM line is presented in [15], However, the scheme's performance is influenced by slip variations in the DFIG wind farm. A protection scheme with low communication capabilities for DFIG wind farms is reported in [16], Nevertheless, it is susceptible to close-in faults and noise conditions. In [17], Superimposed based distance protection for DFIG wind farm integrated line is presented. However, this scheme is does not validate the effect of noise and system parameter variations. The negative sequence and zero sequence based accelerated distance protection is reported in [18], However, this scheme is does not validate with system capacity and wind power variations. A current sign correlation technique for differential protection is presented in [19], However, it does not account for the impact of high fault resistance and external faults on performance. In [20], the modified distance protection approach for DFIG wind farms is implemented. However, this method does not address the impact of close-in faults, noise conditions and CT saturation on its effectiveness. Different methodologies and their gaps are identified and compiled in Table 1.

Table 1. Summary of methodologies and identified research gaps.

Refs.	Methodology	Gaps
[21]	Recursive discrete stock well relaying method	Not validated under system capacity variation.
[22]	Superimposed component, TT transform – decision tree classifier and travelling wave technique	• System configuration changes not considered • Large data is required to train the model
[23]	A transient-based distance protection for DFIG-based wind farms	Not validated under different DFIG operating modes.
[24]	New adaptive relaying algorithm based on synchronized measurement	Impact of different STATCOM modes on relaying scheme is not addressed.
[25]	DWT approach based differential relaying algorithm for STATCOM	Not validated under different modes of operation of STATCOM.
[26]	Least Square transient detector coefficient based fault detection for DFIG line	The impact of parameter variation of DFIG on relaying algorithm is not addressed.
[27]	Differential current ratio relaying algorithm for STATCOM line	Noise condition as well as CT saturation condition are validated.

In [28], the symmetrical component and machine learning based relaying technique for transmission line links DFIG wind farm with TCSC is presented. Nonetheless, the suggested approach excludes considerations like circuit configuration and wind farm rating and machine learning model required the large volume of data. In [29], an improved protection relaying method is suggested for transmission line links DFIG wind farm and TCSC. The method, however, ignores factors like wind rating and various sample frequencies. A teager energy approach based on variational mode decomposition is implemented in [30]. Conversely, the algorithm ignores how noise affects the condition of fault location. In [31], adaptive signal processing and machine earning based relaying strategy for series compensation line with DFIG wind farm is presented. However, this method does not consider the impact of power swing and large data is required to train the model. The
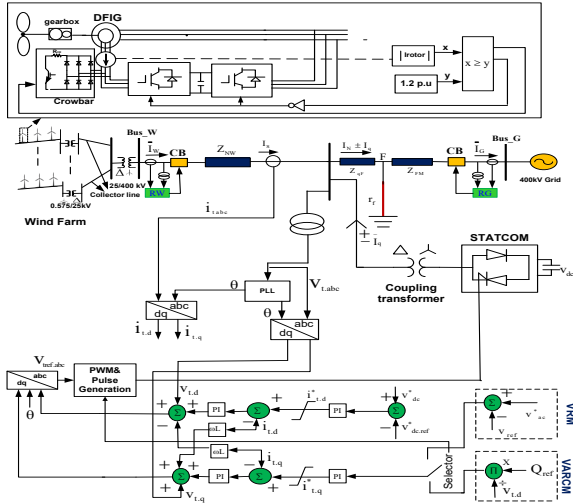
Fig. 1. Schematic illustration of a transmission line with STATCOM Integrated DFIG wind far.
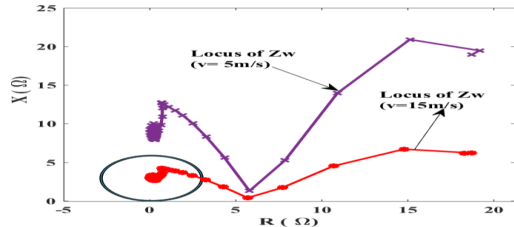

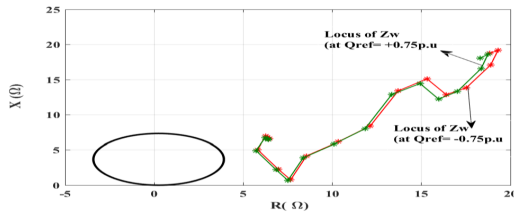Fig. 2. Wind side relay R_w during a AG fault under VRM mode.

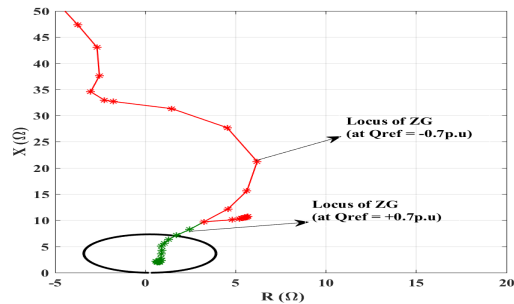Fig. 3. Wind side relay R_w during a three-phase fault under VARCM mode.

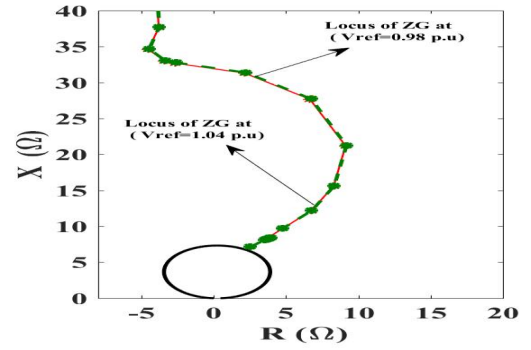Fig. 4. Grid side relay RG during a three-phase fault under VARCM mode.

Fig. 5. Grid side relay RG during a three-phase fault under VRM mode.
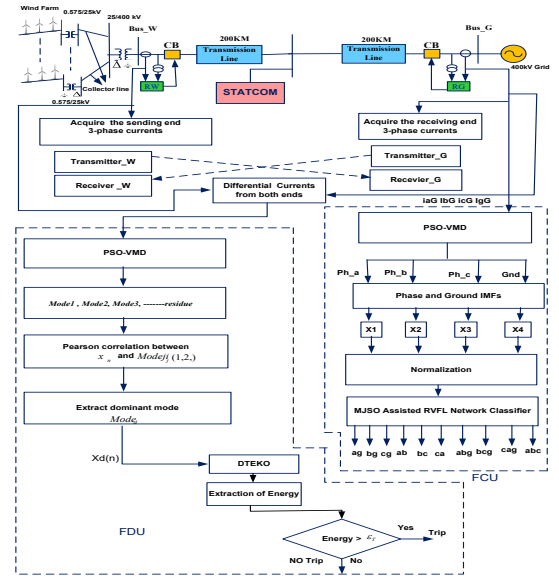

Fig. 6. Proposed relay scheme for transmission line with STATCOM compensation connected to a DFIG-based wind farm.
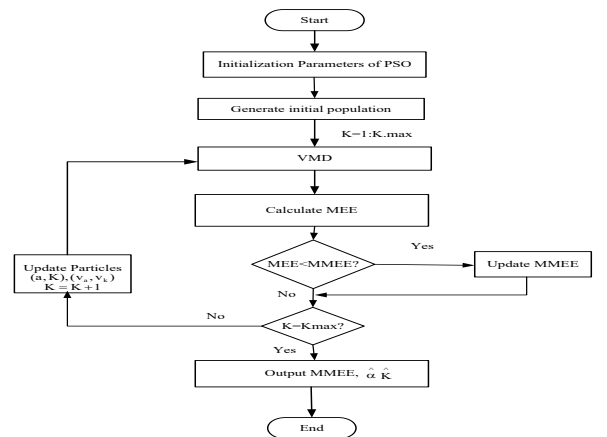

Fig. 7. Flowchart of PSO-VMD algorithm.

artificial intelligence with optimization assisted controller is used to enhance the performance for DFIG wind farm is reported in [32]. However, the large data to train the model is required it leads to computational burden. Improved environmental adaption method based relay coordination for micro grid is presented in

[33]. However, this scheme improved performance is achieved by proper selection the relay characteristics. Data mining and support vector machine based fault diagnosis for modern power system is implemented in [34]. However, this classifier has less no of features and large data is required to train the model it leads to computational burden. The variational mode decomposition is
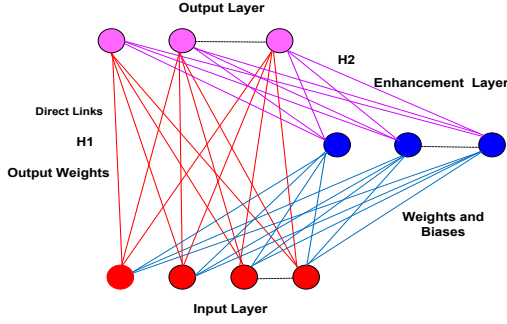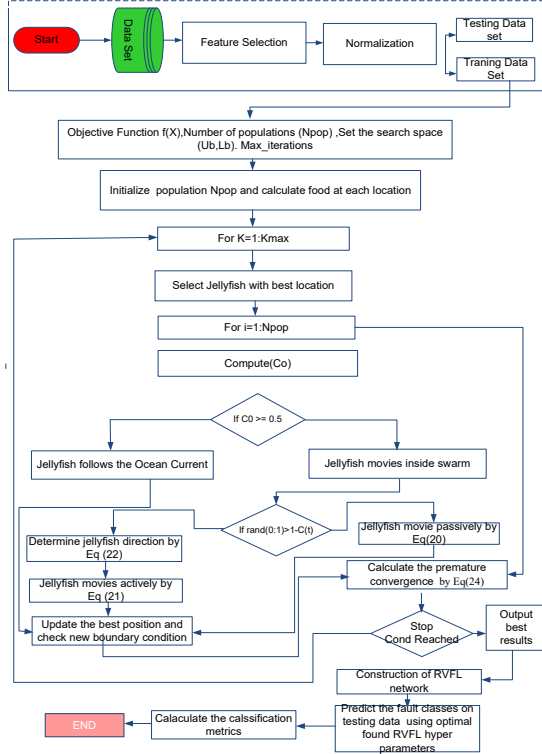
Fig. 8. Architecture of the RVFL network.

Fig. 9. Proposed MJO-RVFLN classifier flowchart.

introduced in [35]. The particle swarm optimization based the variational mode decomposition is reported [36]. Nevertheless, the suggested approach ignores the impact of noise level in vibration signal.

The above aforementioned study indicates that limited papers are reported on fault detection and classification in transmission line connected to DFIG wind farm with STATCOM compensation. Furthermore, the existing approaches need more investigation under challenging conditions such as noisy environments, CT saturation, load switching events and voltage/current inversion. As a result, it is needed to develop a fast, accurate, and reliable protection scheme for fault detection and classification in such a critical transmission system.

To overcome above shortcomings this paper presents an improved protection system for transmission lines that link the DFIG wind farms with STATCOM compensation. The proposed method utilizes fault detection through a combination of partial swarm optimization-assisted variational mode decomposition (PSO-VMD) and Dominant Mode Filtering -Teager Kaiser Energy Operator (DMF-TKEO) technique. For fault classification, it employs PSO-VMD along with a modified Jellyfish optimization-assisted random

vector functional link (MJO-RVFLN) approach.

1.3. Contribution

The primary contributions of the manuscript are summarized as follows:

1) Investigate the potential impacts of STATCOM and DFIG wind farms on a conventional distance relaying-based transmission line protection scheme.

2) A new fault detection is proposed which utilize the Particle Swarm Optimization based Variational Mode Decomposition(PSO-VMD) and Dominant Mode Filtering-Teager Kaiser Energy operator (DMF-TKEO) for fault detection.

3) A new fault classification is proposed which utilize the (PSO-VMD) based Modified Jellyfish Optimization assisted Random Vector Functional Link Network (MJO-RVFLN) for fault classification.

4) A test system with a range of possible faults and non-fault events is used to evaluate the efficacy of the proposed relaying algorithm. This evaluation thoroughly examines the algorithm's performance and reliability under different operating conditions and scenarios.

5) The proposed relaying scheme is validated with different faults, noise condition, CT saturation and different non-fault events.

6) The model performance is significantly enhanced by incorporating energy features as its input and optimizing it hyper parameters.
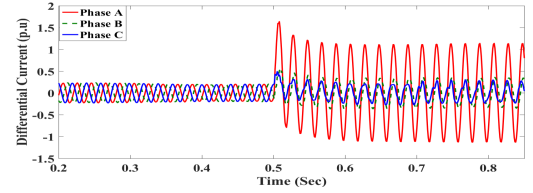

Fig. 10. Differential current in three phases during the AG fault.
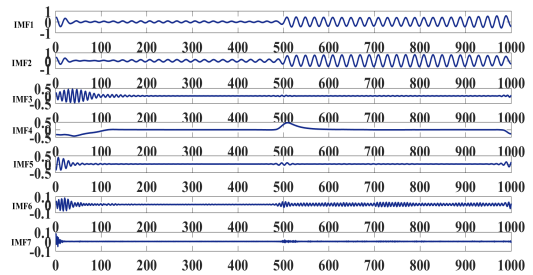

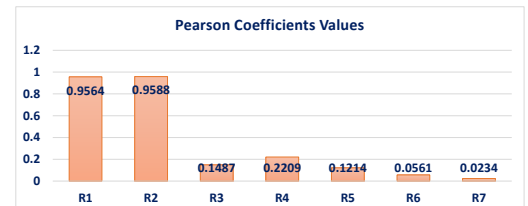Fig. 11. IMFs were extracted through phase-A differential current during the AG fault.

Fig. 12. Values of the Pearson coefficients for various IMF modes.

Table 2. Generation of training and testing data.

Parameters	Data set for training	Data set for testing
Both symmetrical and unsymmetrical faults	Both symmetrical and unsymmetrical faults and no-fault	Both symmetrical and unsymmetrical faults and no-fault
Distance (in km)	10, 60, 120, 180, 240, 300 and 360km (7 cases)	1, 8 (5%), 80 (20%), 160 (40%), 240 (60%) and 320km (80%) from grid side (6 cases)
Angle of fault inception ($°$)	0, 60, 120, . . . , 300° with increment of 60 (6 cases)	0, 60, 90, 144, and 180° (5 cases)
Resistance of fault (R_f)	10, 20, . . . , 80Ω with increment of 20 (5 cases)	1, 10, and 100Ω (3 cases)
Mode of operation	VRM and VARCM (2 cases)	VRM and VARCM (2 cases)
Wind speed (m/s)	2, 4, 6, and 8 m/s (4 cases)	5, 10, and 15 m/s (3 cases)
Total no. of patterns	$10 \times 7 \times 6 \times 5 \times 2 \times 4 = 16800$	$10 \times 6 \times 5 \times 3 \times 2 \times 3 = 5400$
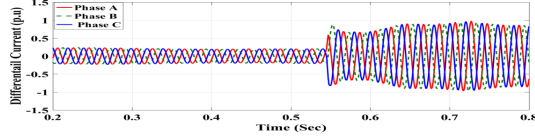
Fig. 13. Differential Currents during a three phase fault.
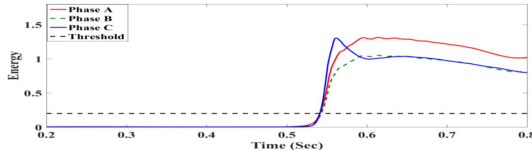
Fig. 14. Performance during a three phase fault.
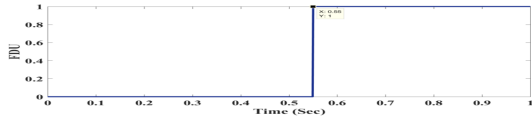
Fig. 15. Results of proposed fault detection unit.
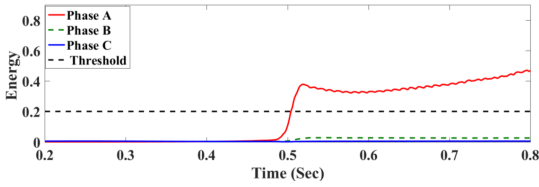
Fig. 16. Performance during a single phase fault.
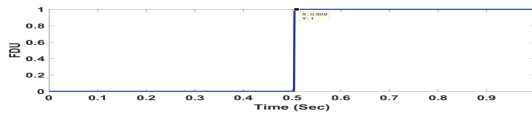
Fig. 17. Results of proposed fault detection unit.
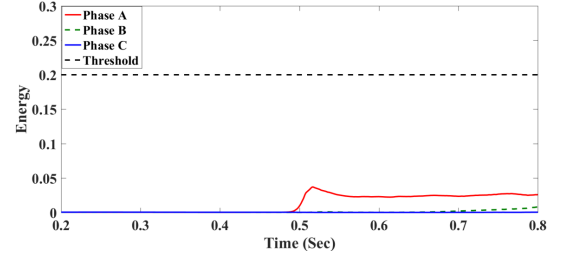
Fig. 18. Performance on Inductive load switching.
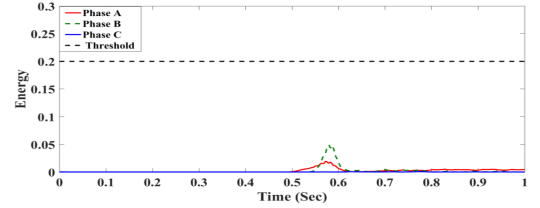
Fig. 19. Performance on capacitive load switching.
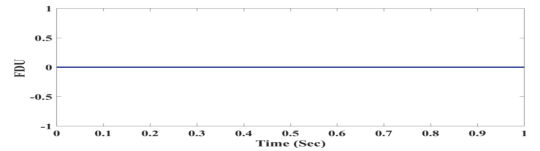
Fig. 20. Results of proposed fault detection unit.
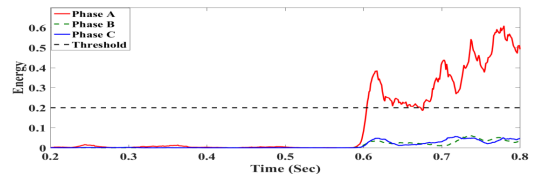
Fig. 21. Perfromance on AG fault during noise condition.
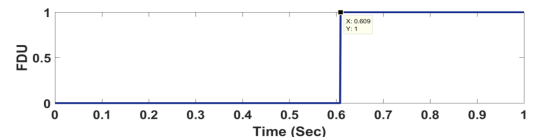
Fig. 22. Results of proposed fault detection unit.

1.4. Organization

The paper structure is as follows: The impact of distance relay malfunctions on transmission lines that link the DFIG wind farms with STATCOM compensation is investigated in Section 2. Section 3 describes the implementation of the system and methodology. Section 4 discusses the implementation of the proposed technique. Section 5 shows results and discussions. Section 6 presents the comprehensive comparison of the existing methodologies. Lastly, section 7 provides the conclusions.
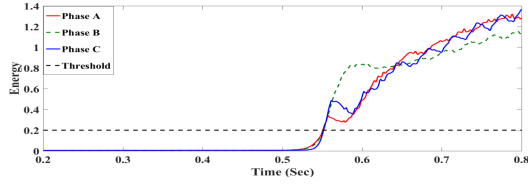
Fig. 23. Performance on three phase fault during CT saturation.
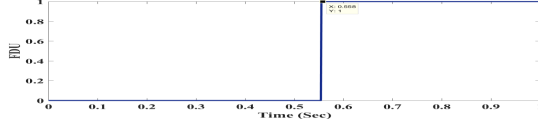
Fig. 24. Results of proposed fault detection unit.
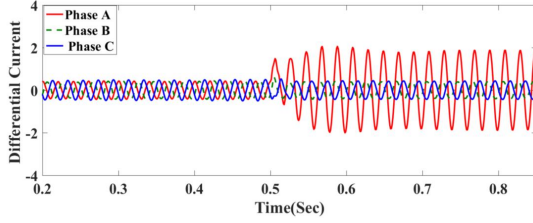
Fig. 25. Differential current during AG fault of double circuit line.
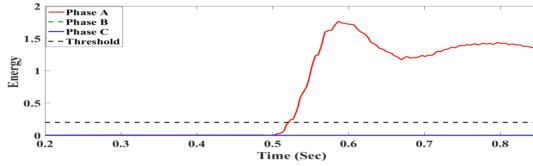
Fig. 26. Performance on AG fault during double circuit condition.
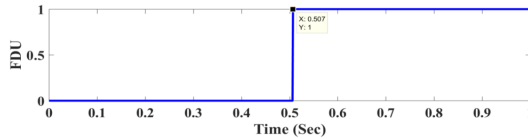
Fig. 27. Results of proposed fault detection unit.
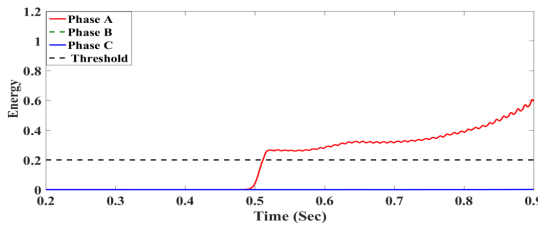
Fig. 28. Performance on AG fault during high source impedance ratio.
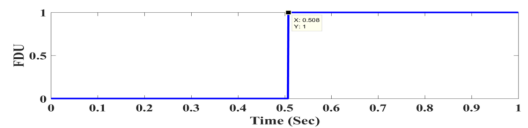
Fig. 29. Response of fault detection unit.

Fig. 30. Magnitude of Voltage of MMG system during all cases for loss reduction.
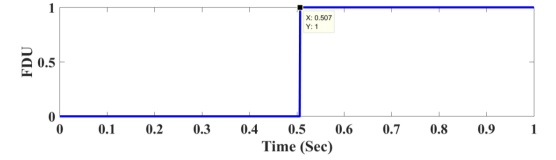
Fig. 31. Response of fault detection unit.
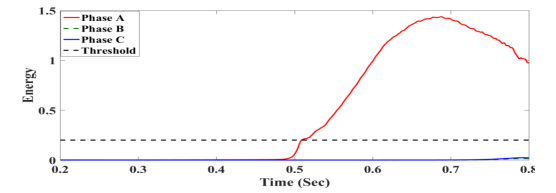
Fig. 32. Performance on AG fault during low source impedance ratio.
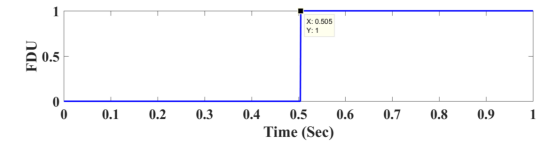
Fig. 33. Response of fault detection unit.
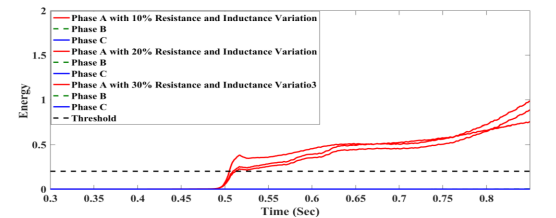
Fig. 34. Performance on AG fault during transmission line parameter variation.

Fig. 35. Response of fault detection unit

2. INVESTIGATION OF MAL-OPERATIONS OF DISTANCE RELAYS ON TRANSMISSION LINES THAT LINK THE DFIG WIND FARMS WITH STATCOM COMPENSATION
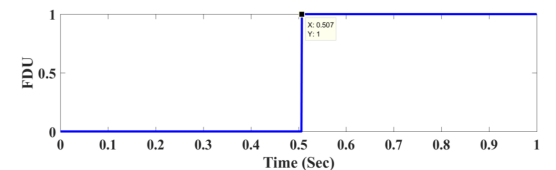
To evaluate the performance of the distance relays, the Fig. 1, is simulated using MATLAB/Simulink. The ratings for the components and parameters are detailed in Appendix A.

Fig. 1 shows that, due to low zero-sequence impedance offered by wind farm the larger zero-sequence current is produced once the ground fault occurs on the line. The DFIG wind farms have Low Voltage Ride Through (LVRT) Capability due that when a ground fault occurs on line, it produces a low fault current but contributes
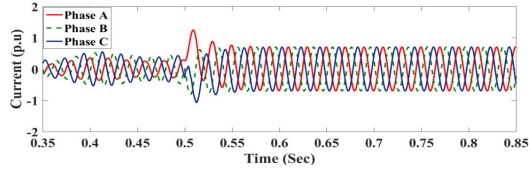
Fig. 36. Grid side relay R_G currents during the three phase fault.
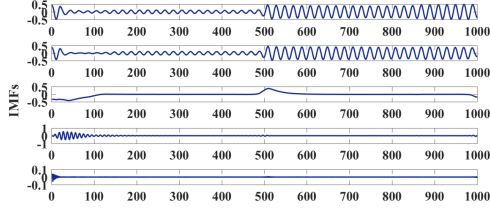
Fig. 37. IMF extraction of phase A current on the grid side during the three-phase fault.
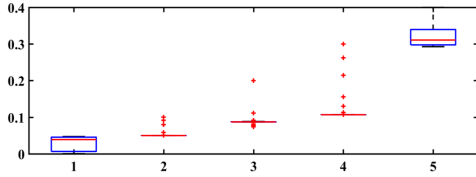
Fig. 38. Extracted IMFs box plot.
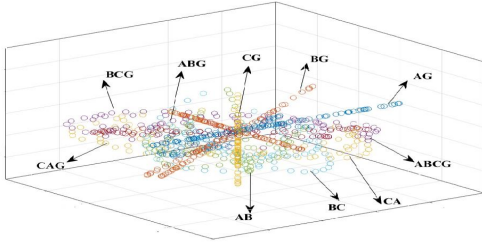
Fig. 39. Feature data set for various fault types.
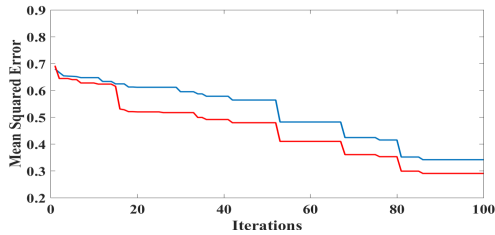
Fig. 40. Convergace curve of MJO-RVFLN and PSO-RVFLN.
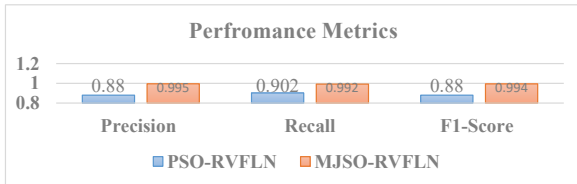
Fig. 41. Performance indicators for the proposed PSO-RVFLN and MJO-RVFLN.

a high magnitude of zero-sequence current which can affect the performance of wind side relay. As show in Fig. 1 the STATCOM

Table 3. Algorithm parameters of the MJO algorithm.

	Parameters	Values
MJO	Time control (C_o)	0.5
	Logistic chaotic constant (A)	4.0
	Motion coefficient (I)	0.1
	Distribution coefficient	3.0
	Number of populations (N_{pop})	50
	Maximum iteration (Max_iter)	100

Table 4. RVFL network hyper parameters.

Hyperparameters	Values
Number of hidden neurons	[100, 1000]
Bias of the network	[0, 1]
Scale mode of the network	[1, 3]
Scale of the network	[0.0001, 0.9999]

is used to improve the line power transfer capability and voltage stability. The STATCOM have two mode of operation first one is Voltage Regulator Mode (VRM) and second one is VAR control mode (VARCM). Due to the modulation of STATCOM mode of operation, the impedance varies, which affects the distance relay operation [22].

2.1. Effect of the relay on the wind side

The relay R_w impedance is expressed as follows:

$$Z_w = Z_{Nq} + (1 \pm \frac{I_q}{I_N})Z_{qf} + (1 + \frac{I_m \pm I_q}{I_N})r_f \qquad (1)$$

Consider the R_w performance, an AG fault was introduced at 90% of the line distance (360km) from the wind-side relay R_w at 0.5 seconds, with R_f of 10Ω, the wind speed at 15 m/s and VRM mode with a V_{ref} of 1.0p.u. The results are illustrated in Fig. 2. The relay R_w seen an apparent impedance of $Z_{Appw} = (V_{a(w)}/Ia_{(w)} + K_0 I_{0(w)})$. Consequently, the Z_{APPw} locus enters zone 1 of the relay R_w. In this situation the relay loses it discrimination. Conversely, when the wind speed is (v) is 5 m/s, the output power decreases, resulting in reduced zero-sequence current. Consequently, the locus of the Z_{APPw} lies outside of zone 1, as illustrated in Fig. 2. Both of these scenarios impact the performance of the wind-side relay R_w.

Further, to test the wind side relay R_w performance a three phase fault is created at 70% of the line (280Km) after STATCOM, with fault resistance is 10Ω, wind speed is 15m/s and 5 m/s and VARCM mode with Q_{ref} (+0.75p.u to -0.75p.u) as shown in Fig. 3.

2.2. Effect of the relay on the grid side

In the first case, a 3-phase fault was produced at 70% (280km) from the grid-side relay R_G and in VARCM mode with Q_{ref} (+0.7p.u to -0.7p.u), as shown in Fig. 4. It indicates that the Z_{AppG} seen by relay is either increased or decreased due to injection/absorption of reactive power to/from the transmission line. Second case the 3-phase fault is produced at (80%) (320km) away from R_G and VRM mode with V_{ref} (1. 04p.u to 0. 98p.u) as shown in Fig. 5. It indicates that the apparent impedance Z_{AppG} differs from the actual impedance and grid side relay pose to under reach/over reach. According to the aforementioned analysis, there is an impact on the distance relays performance from both ends of the transmission line that are linked to the DFIG with STATCOM. Because of this, it requires an advanced relaying scheme to protecting that vital transmission lines.

Table 5. PSO tuned hyperparametrs optimal RVFL network.

No of neurons in input layer	No of neurons in Hidden layer	No of neurons in output layer
4	820	10

Table 6. MJO tuned hyperparameter Optimal RVFL network.

No of neurons in input layer	No of neurons in Hidden layer	No of neurons in output layer
4	540	10

3. SYSTEM STUDIED AND METHODOLOGY

The proposed relaying scheme is tested against various faults and system operating conditions, as demonstrated in Fig. 6. A sampling frequency of 8kHz is selected for the simulation study.

3.1. PSO-VMD-DMF-TKEO based fault detection algorithm

Step 1: Data acquisition

The three phase currents (p.u) are obtained from the both ends of the STATCOM-DFIG transmission line.

Step 2: Determine each phase differential current (I_{diff}).

Step 3: Advanced signal processing:

Using the Particle Swarm Optimization based variation mode decomposition (PSO-VMD) technique to extracted the different modes (IMFs) from the differential current (I_{diff}).

Step 4: Determination of pearson correlation coefficients.

Calculate the pearson correlation coefficient, using Eq. (9) for all IMFs. Then, set rd $\approx$ 1 to the index of the $mode_d$ IMF (i.e. $mode_d$).

Step 5: Determination of dominant mode:

The highest magnitude one is selected as dominant mode ($mode_d$) among the all Pearson coefficients of IMFs.

Step 6: Apply the teager kaiser energy operator.

The teager kaiser energy operator is applied to dominant mode ($mode_d$ IMF) to compute the energy.

Step 7: Fault detection unit:

If Energy $\psi(k) \succ \varepsilon_T$ then trip.

Otherwise no trip.

3.2. MJO-RVFLN classifier based fault classification algorithm

Step 1: Data acquisition:

To acquire the grid side relay currents.

Step 2: Advanced signal processing technique:

The grid side relay currents are passed through the PSO-VMD technique to extraction of phase and ground IMFs.

Step 3: Determination of energy:

To compute each phase IMF and ground IMF energy.

Step 4: Inputs to proposed modified jellyfish-RVFLN classifier.

Each phase and ground energy is given to proposed classifier.

Step 5: Fault classification unit:

Classification of symmetrical and unsymmetrical faults using MJO-RVFLN classifier.

4. PROPOSED FAULT DETECTION AND CLASSIFICATION APPROACH

The proposed fault detection and classification the computational steps are incorporated in this section for quick and reliable fault detection/classification of STATCOM compensated DFIG wind farm line.

4.1. Proposed fault detection (PSO-VMD-DMF-TKEO) approach

The following sections are describing the detail of theoretical frame work of fault detection approach.

A) Variational mode decomposition

In the late 1990s, Huang introduced the Empirical Mode Decomposition (EMD) method, which separates a signal into different spectral bands and independent modes of unknown origin. However, EMD has limitations, particularly its sensitivity to noise and sampling issues. A newer signal processing technique, known as Variational Mode Decomposition (VMD), has been developed to decompose signals into band-limited intrinsic mode functions (IMFs). VMD offers advantages over methods like Wavelet Transform (WT) and the Huang-Hilbert Transform (HHT), such as eliminating mode aliasing and reducing sensitivity to noise. The mathematical principles underlying variational mode decomposition [35], are explained below.

Unlike EMD and EEMD, VMD is a self-adaptive, quasi-orthogonal signal processing technique that is fully non-recursive [37]. The VMD method is built upon principles such as heterodyne demodulation, the Hilbert transform, and traditional Wiener filtering [35].

By using the VMD algorithm, the signal x(t) can be divided into K modes, or sub signals $u_k(n)$, each of which is compact around a central point $w_k(t)$. The representation of x(t) is as follows [35].

$$x(t) = \sum_{i=1}^{k} \mathrm{mode}_i(t) + res(n) \quad (2)$$

Moreover, the VMD technique requires the minimization of a constrained variational problem involving the sum of the bandwidths of each mode component.

Consequently, the constrained variational problem's mathematical model is as follows [35, 36]:

$$\min_{\{u_k\},\{w_k\}} \left\{ \sum_{k=1}^{k} ||\partial t \left\{ \left[\delta(t) + \frac{j}{\Pi t} \right] * u_k(t) \right\} e^{-jw_k t} || \frac{2}{2} \right\}$$
$$s.t. \sum_k \{u_k(t)\} = x(t)$$
$$(3)$$

Where $u_k = \{u_1, u_2, \ldots \ldots u_k\}$ represents the modal function vector, and $w_k = \{w_1, w_2, \ldots \ldots w_k\}$ represents the central frequency vector.

The constraint problem needs to be converted into an unconstrained problem. To do this, the quadratic penalty factor η and lagrangian multiplier $\lambda(t)$ are introduced. Finally, the following is the expression for the unconstrained variational problem is express as follows.

$$\tau(u_k, w_k, \lambda) = \eta \sum_{k=1} ||\partial t \left\{ \left[\delta(t) + \frac{j}{\pi t} \right] * u_k(t) \right\} e^{-jw_k t} || \frac{2}{2}$$
$$+ ||x(t) - \sum u_k(t)|| \frac{2}{2}$$
$$+ \langle \lambda(t), x(t) - \sum u_k(t) \rangle$$
$$(4)$$

To resolve this unconstrained problem, the following steps are implemented:

Algorithm of VMD:

1) Initialize:

$$\{u^1{}_k\}, \{w^1{}_k\}, \lambda^1, n = 0$$

2) repeat

3) $n \leftarrow n + 1$

4) for $k = 1$ to k do

5) Update u_k for all $w \geq 0$:

6) $u_k{}^{n+1} \leftarrow \arg_{\{u_k\}} \min \Gamma \left(\{u^{n+1}{}_{i \prec k}\}, \{u^{n+1}{}_{i \geq k}\}, \{w^n{}_i\}, \{\lambda^n\} \right)$

7) Update w_k

Table 7. Proposed MJO-RVFLN classifier test results.

Type of fault	Location of fault	Resistance of fault (Ω)	STATCOM Modes	Wind Speed (m/s)	Fault Inception Angle (°)	Fault classification time (ms)	MJO-RVFLN Classified as
AG	Before STATCOM	30	VRM	5	45	6	AG
ABG	Before STATCOM	100	VRM	20	140	5	ABG
AB	Before STATCOM	60	VRM	15	90	8	AB
ABC	Before STATCOM	150	VRM	10	160	6	ABC
AG	After STATCOM	260	VARCM	10	60	9	AG
BCG	After STATCOM	360	VARCM	5	180	8	BCG
BC	After STATCOM	280	VARCM	10	90	7	BC
ABC	After STATCOM	320	VARCM	15	180	9	ABC

Table 8. Percentage accuracy and confusion matrix of the proposed MJO-RVFLN classifier.

Fault type	1	2	3	4	5	6	7	8	9	10	Proposed MJO-RVFLN (%) classification accuracy
1	539						1				99.98
2		539						1			99.98
3			536			2			2		99.94
4				537		3					99.95
5					540						100.00
6						538	2				99.97
7	2						538				99.97
8		1						539			99.98
9			1			2			537		99.95
10			2							538	99.97
						Total average percentage accuracy					**99.97**

8) $w_k{}^{n+1} \leftarrow \arg_{\{w_k\}} \min \Gamma \left(\{u^n{}_i\}, \{w^{n+1}{}_{i \prec k}\}, \{w^{n+1}{}_{i \geq k}, \{\lambda^n\}\right)$

9) **Update** λ^n :

10) $\lambda^{n+1} \leftarrow \lambda^n + \tau \left(f + \sum_k u_k{}^{n+1}\right)$

11) **end for**

12) **Until convergence** $\sum_k ||u_k{}^{n+1} - u_k{}^n||_2^2 / ||u_k{}^n||_2^2 \prec \varepsilon$

B) Variational mode decomposition using particle swarm optimization (PSO-VMD)

Variational Mode Decomposition (VMD) [35], operates on the premise that each intrinsic mode has a limited bandwidth defined by specific values of α and K. Selecting the appropriate parameters is crucial for VMD's effective signal decomposition. Unlike "empirical" methods such as EMD and LMD, VMD offers a high degree of self-adaptability, particularly for nonstationary and nonlinear signals. However, the complexity of signal characteristics makes it challenging to manually determine the optimal α and K values. Additionally, employing grid search (GS) to identify the best parameters globally can be time-consuming [36].

Kennedy and Eberhart [38, 39] introduced the Particle Swarm Optimization (PSO) algorithm, a stochastic, population-based technique for solving both discrete and continuous optimization problems. Each particle position in PSO reflects a possible way to solve the optimization problem. Particles adjust their velocities based on rules inspired by bird flocking behavior, seeking improved positions within the search space. Defining an appropriate optimality function is crucial for effective PSO implementation, within the PSO framework, the optimality function in this study is the minimum mean envelope entropy (MMEE). The MMEE is formulated as follows [37].

$$\langle \alpha, K \rangle = \begin{array}{c} \arg \min \\ (\alpha, K) \end{array} \left\{ \frac{1}{K} \sum_{i=1}^{K} H_{en}(i) \right\} \quad (5)$$

where α, K are the quadratic penalty factor and no of modes and H_{en} is envelop entropy of each mode u_k, and the envelop entropy is represented as follows:

$$H_{en}(i) = -\sum_{i=1}^{K} p_i \log_2(p_i) \quad (6)$$

Where p_i is normalized envelop of each mode u_k.

The flowchart for the proposed PSO-VMD technique is shown in Fig. 7 [36], which can be described through the following steps. First, the PSO initialization parameters are set, including the migration velocities (v_a, v_b) of the particles, the population size (α_1, K_1), and the number of iterations (K_{max}). For this instance, parameters are set as $K_{max} = 50$, $\alpha_1 = 60$, $K_1 = 1$, $v_a = 20$, and $v_b = 1$ [36]. Next, the VMD technique is applied using these PSO initialization parameters to compute the MEE of the subcomponents. Then, the positions and velocities of all particles in the population are updated based on Eq. (7), where δ is the inertia weight, and C_1 and C_2 control the particles' movement. The random number rand varies between 0 and 1, and K_{id} and α_{id} refer to the particles' current positions and the best historical positions, respectively. In this study, C_1 and C_2 are set to 0.5, and δ is set to 1. If the current MEE fitness value is better than the previously recorded best fitness value (MMEE) as given in Eq. (8), the positions and velocities of the particles are updated. The process continues until K reaches K_{max}, at which point the algorithm concludes with the final optimal values, including MMEE, $\hat{\alpha}$, and $\hat{K}$.

$$\begin{bmatrix} \hat{\alpha} \\ \hat{K} \end{bmatrix} = \delta * \begin{bmatrix} \alpha_{id} \\ K_{id} \end{bmatrix} + \\ C_1 * Rand(0, 1) * (\tilde{\alpha}_{id} - \alpha_{id}) + \\ C_2 * Rand(0, 1) * (\hat{K}_{id} - K_{id}) \quad (7)$$

$$\hat{\alpha}_{id} = \hat{\alpha}, \hat{K}_{id} = \hat{K} \quad (8)$$

C) Dominant Mode Filtering (DMF) algorithm

The Dominant mode filtering algorithm can be implemented as follows:

Step 1: The PSO-VMD is applied to differential current to extract the set of modes (IMFs).

Step 2: As many times as there are modes, pearson correlation coefficient is calculated using Eq. (9) and then

Table 9. Proposed MJO-RVFLN classifier test results.

SNR (dB)	Type of fault	Location of fault in km		Resistance of fault in (Ω)	STATCOM modes	Wind speed (m/s)	Fault inception angle (°)	Fault classification time (T_1) (ms)	MJO-RVFLN classified as
	AG		40	3	VRM	10	30	5	AG
	ABG	Before STATCOM	90	15		15	120	6	ABG
	AB		70	60		5	80	8	AB
20	ABC		120	5		15	140	6	ABC
	AG		240	10	VARCM	10	45	9	AG
	BCG	After STATCOM	330	30		5	160	9	BCG
	BC		260	100		15	60	8	BC
	ABC		300	15		10	100	7	ABC

Table 10. Percentage accuracy and confusion matrix of the proposed MJO-RVFLN classifier.

Fault type	1	2	3	4	5	6	7	8	9	10	Proposed MJO-RVFLN (%) classification accuracy
1	536					4					99.25
2		538							2		99.62
3			535		3				2		99.07
4				533		6					98.70
5					539				1		99.81
6						540					100.00
7	3						537				99.44
8		2						538			99.62
9		3					3		534		98.88
10		2	3							535	99.07
				Total average percentage accuracy							**99.34**

the correlation coeffient $r(x(n), \text{mode}_k(n)) \simeq 1$ indexes the dominant $Mode_d$.

$$r(x(n), \text{mode}_k(n)) = \frac{\sum_n \left[(x(n) - m_x)(\text{ mod } e_k(n) - m_y) \right]}{\sqrt{\sum_n (x(n) - m_x)^2} \sqrt{\sum_n (\text{ mod } e_k(n) - m_y)^2}} \quad (9)$$

The correlation coefficient between the input signal X(n) and each of the IMFs is expressed as follows:

$$\rho_i = [\rho_{iIMF1}, \rho_{2IMF2}, - - - - - - - - - - -, \rho_{3_{IMFn}}]$$

Where x(n) original signal and each mode or IMF is represented by $mode_k$(n).

Step 3: The dominant $mode_d$ x_d(n) is passed thought the Teager Kaiser Energy Operator from which determine the energy and it is used for fault detection.

D) Teager kaiser energy operator based fault detection

The Teager Kaiser Energy Operator (TKEO) was initially used in AM-FM demodulation. Moreover, TKEO has been used to speech signals, transient calculations, and noise separation etc.

For continuous time signal the x_c(t), the TKEO is defined as:

$$\Psi[x_c(t)] = \dot{x_c(t)} - x_c(t)\ddot{x_c(t)} \quad (10)$$

$\dot{x_c(t)}$ is the first derivative and $\ddot{x_c(t)}$ is second derivative of x(t).Teager Kaiser Energy Operator can be expressed in discrete as:

$$\Psi[x_c(n)] = x_c(n)^2 - x_c(n-1)x(n+1) \quad (11)$$

For fault detection, the resulted signal x_c(n) is passed in to Teager Kaiser Energy Operator in Eq. (11) to compute the energy from which to identify the fault detection.

If $\Psi[x_c(n)] < \varepsilon_T$ fault is not detected, then no-trip

If $\Psi[x_c(n)] > \varepsilon_T$ fault is detected, then trip

4.2. Proposed fault classifier (PSO-VMD based MJO-RVFLN)

Due to the power electronics interfacing with both DFIG wind turbines and STATCOM, the fault current patterns near the wind farm side are quite different from those at a standard synchronous generator terminal. This discrepancy can lead to incorrect fault classifications by distance relays situated close to the wind farm. To address this issue, this article introduces a PSO-VMD-based MJO-RVFLN algorithm for fault classification, utilizing local grid current measurements. The following sections provide details on the proposed fault classifier.

A) RVFL network

RVFLN is a variation of a single hidden layer feedforward neural network (SLFN) that uses randomization. It consists of three layers: input, hidden, and output, all of which contain neurons connected by weights. To bypass the backpropagation algorithm, the weights between the input and hidden layers are randomly assigned from a specified range and remain fixed during training. The output weights are then determined analytically using the least squares method or pseudo-inverse method. In RVFLN, the original features are directly connected to the output layer through direct links [40]. The RVFLN generalization performance is enhanced by the direct links. Fig. 8 illustrates the architecture of the RVFL network.

The RVFLN model mathematically represented as, $f : R^d \to R^c$ can be written as:

$$\begin{aligned} f(x_i) &= \sum_{k=1}^{d} \beta_k x_{ik} + \\ &\sum_{k=d+1}^{L} \beta_k \theta \left(\langle \mu_k, x_i \rangle + \sigma_k \right), i = 1, 2, \dots N \end{aligned} \quad (12)$$

The standard inner product of $\langle \mu_k, x_i \rangle = \mu_k . x_i$ is defined in Euclidean space R^d.

The optimization problem of RVFLN model with L no of hidden neurons as follows:

$$\min_{\beta} \; \frac{1}{2} \parallel \beta \parallel^2 + \frac{1}{2} C \parallel \xi \parallel^2 \quad (13)$$

Subjected to $H\beta - Y = \xi$

Where $\parallel . \parallel$ standard frobenius norm and $\xi = [\xi_1, \xi_2, \dots \xi_N]^T$ is error term corresponding to N samples. β and H are represent the output weight matrix and the concatenation matrix, which combines the input data with the output from the hidden layer, respectively and Y is target matrix.

The optimization problem Eq. (13) can written as:

$$\min_{\beta \in R^{(d+L) \times c}} \; \frac{1}{2} \parallel \beta \parallel^2 + \frac{1}{2} C \parallel H\beta - Y \parallel^2 \quad (14)$$

here

$$H = [H_1 H_2]_{N \times (d \times L)}$$

Where

Table 11. Proposed MJO-RVFLN classifier test results.

SNR (dB)	Type of fault	Location of fault in km		Resistance of fault in (Ω)	STATCOM modes	Wind speed (m/s)	Fault inception angle (°)	Fault classification time (T_1) (ms)	MJO-RVFLN classified as
	AG		30	5	VRM	5	60	6	AG
	ABG	Before STATCOM	80	10		10	80	7	ABG
	AB		100	30		15	120	8	AB
30	ABC		140	45		10	140	8	ABC
	AG		230	30	VARCM	15	30	5	AG
	BCG	After STATCOM	270	15		10	180	8	BCG
	BC		300	80		5	60	9	BC
	ABC		330	20		15	140	7	ABC

Table 12. Percentage accuracy and confusion matrix of the proposed MJO-RVFLN classifier.

Fault type	1	2	3	4	5	6	7	8	9	10	Proposed MJO-RVFLN (%) classification accuracy
1	535					5					99.07
2		533					7				99.70
3			535			2		3			99.07
4				536			4				99.25
5					539	1					99.81
6						540					100.00
7	3						537				99.44
8		6						534			98.88
9			3				3		534		98.88
10				3						537	99.44
				Total average percentage accuracy							**99.25**

$$H_1 = \begin{bmatrix} x_{11} & .. & x_{1d} \\ : & : & : \\ x_{N1} & .. & x_{Nd} \end{bmatrix}_{N \times d}$$

and

$$H_2 = \begin{bmatrix} \theta(\mu_1.x_1 + \sigma_1) & .. & \theta(\mu_L.x_1 + \sigma_L) \\ : & : & : \\ \theta(\mu_1.x_N + \sigma_1) & .. & \theta(\mu_L.x_N + \sigma_L) \end{bmatrix}_{N \times L} \tag{15}$$

$$\beta = \begin{bmatrix} \beta_1 \\ \beta_2 \\ \beta_{(d+L)} \end{bmatrix}_{(d+L) \times c}$$

$$and \tag{16}$$

$$Y = \begin{bmatrix} y_1 \\ y_2 \\ y_N \end{bmatrix}_{N \times c}$$

Here $\beta_k = \begin{bmatrix} \beta_{k1} & \beta_{k2} & \beta_{kc} \end{bmatrix}$ is the outputs weight matrix with K^{th} hidden node and output node. where $1 \leq k \leq d + L$ and $\mu_j = \begin{bmatrix} \mu_{j1} & \mu_{j2} & \mu_{jd} \end{bmatrix}$ is the weight vector that connects the j-th hidden node to the input nodes. $x_i = \begin{bmatrix} x_{i1} & x_{i2} & x_{id} \end{bmatrix}$ is the i-th sample .For target matrix $y_i = \begin{bmatrix} y_{i1} & y_{i2} & y_{ic} \end{bmatrix}$, $1 \leq i \leq N$.

The optimal solution of the problem Eq. (13) ,when $\delta = \frac{1}{c} = 0$ as follows:

$$\beta = H^+ Y \tag{17}$$

where $H+$ denotes the Moore-Penrose generalized inverse of the matrix H [40]. The regularization term is used to prevent overfitting.

B) Modified jellyfish optimization algorithm

The artificial jellyfish search optimizer (JSO), introduced by Chou and Troung [41], is inspired by the foraging behavior of jellyfish in the ocean. The JSO mimics how jellyfish follow ocean currents or move in groups, alternating between these two behaviors using a temporal control system.

The JSO algorithm, in particular, benefits from the logistic map [42], which is mathematically defined as follows:

$$\overrightarrow{X_{i+1}} = \lambda X_i(1 - X_i), \ 0 \leq \overrightarrow{X_0} \leq 1 \tag{18}$$

The logistic chaotic values for the ith jellyfish are stored in the vector X_i Initially, the jellyfish vector X_0 is randomly generated within the range of 0 to 1, with the parameter set to 4 [41]. Following initialization, the jellyfish with the best fitness value is designated as X, representing the most favorable food source. Then, each jellyfish's current location is updated based on the ocean current, as indicated by the expression that follows [41].

$$\overrightarrow{X}_i(t + 1) = \overrightarrow{X}_i(t) + \overrightarrow{r}. * (\overrightarrow{X} * -\beta * r1 * \mu) \tag{19}$$

Where r is 0 to 1, $. *$ is vector manipulation β, is the distribution coeffient and taken as 3. μ is the mean of population r_1 is random number between 0 to 1.

The control mechanism divides the moments within the swarm of jellyfish into two motions which are expressed as follows:

$$\overrightarrow{X}_i(t + 1) = \overrightarrow{X}_i(t) + r_3 * \alpha * (U_b - L_b) \tag{20}$$

The length of the motion is indicated by r_3, which is a random value between 0 and 1. The search space upper and lower bounds are denoted by U_b and L_b. The following is a mathematical description of the formulation of the active motion.

$$\overrightarrow{X}_i(t + 1) = X_i(t) + \overrightarrow{r} * \overrightarrow{D} \tag{21}$$

The vector denoted by r is composed of random numbers ranging from 0 to 1. Where D is the jellyfish's current direction of motion, which is expressed as follows:

$$\overrightarrow{D} = \left\{ \begin{array}{l} \overrightarrow{X}_i(t) - \overrightarrow{X}_j(t), if \ f(\overrightarrow{X}_i) < f(\overrightarrow{X}_j) \\ otherwise \\ \overrightarrow{X}_j(t) - \overrightarrow{X}_i(t) \end{array} \right. \tag{22}$$

where f is the fitness function and j is the jellyfish index at random. The ocean current, passive, and active motions are all switched between by the time control mechanism, which consists of a constant c(t) and a time control function that may be expressed mathematically as follows:

$$c(t) = (1 - t/t_{\max}) * (2 * r - 1) \tag{23}$$

where r is a random number between 0 and 1, t is the current evaluation, and tmax is the maximum evaluation. The jellyfish swim passively or actively within the swam when c(t) $\geq$ c(0); otherwise, they follow the ocean current. Passive motion is applied to the present jellyfish when a random value, r, generated randomly between 0 and 1, is greater than (1 - c(t)); otherwise, active motions are carried out.

The JSO is enhanced by integrating a novel technique that improves both exploration and exploitation capabilities, resulting in the Modified Jellyfish Search Optimization Algorithm. This approach is specifically used for hyper parameter optimization in the RVFLN classifier.

Table 13. Proposed MJO-RVFLN classifier test results.

SNR (dB)	Type of fault	Location of fault in km		Resistance of fault in (Ω)	STATCOM modes	Wind speed (m/s)	Fault inception angle (°)	Fault classification time (T_1) (ms)	MJO-RVFLN classified as
	AG		60	3	VRM	10	30	5	AG
	ABG	Before STATCOM	80	15		15	120	6	ABG
	AB		90	60		5	80	8	AB
40	ABC		140	5		15	140	6	ABC
	AG		240	10	VARCM	10	45	9	AG
	BCG	After STATCOM	330	30		5	160	9	BCG
	BC		260	100		15	60	8	BC
	ABC		300	15		10	100	7	ABC

Table 14. Percentage accuracy and confusion matrix of the proposed MJO-RVFLN classifier.

Fault type	1	2	3	4	5	6	7	8	9	10	Proposed MJO-RVFLN (%) classification accuracy
1	537						3				99.44
2		536							4		99.25
3			534		4	2					98.80
4				532		4			4		98.51
5					538				2		99.62
6						539	1				99.81
7	4						536				99.25
8		2						538			99.62
9		4			4				532		98.51
10		2		4						534	98.88
				Total average percentage accuracy							99.16

This innovative approach, referred to as the Premature Convergence Strategy (PCS), utilizes a control variable to balance between exploiting the method to speed up convergence towards the optimal solution and exploring to reduce the risk of falling into local minima [43]. The mathematical formulation of the premature convergence method is as follows:

$$\vec{X}_i(t+1) = \vec{X}_i(t) + r * (\vec{X}_{r_1}(t) - X_{r_2}(t)) + (1 - r) * (X - X_{r_3}(t))$$

where r is the control parameter and r_1, r_2, and r_3 are the indices of three solutions chosen at random from the population.

5. RESULT AND DISCUSSIONS

To assess the effectiveness of the proposed protection method, the various faults with different system operating modes are simulated in Fig. 6. The generated fault data is then applied for fault detection and classification.

5.1. Results of PSO-VMD-DMF-TKEO based fault detection method

For demonstration, an AG fault is simulated, and the differential current is extracted using the currents from both the sending and receiving ends, as illustrated in Fig. 10. The PSO-VMD analysis indicates that the optimal no of modes (K) is 7, with a value of α is 1968, as shown in Fig. 11.

The Pearson coefficients for each of the IMFs for the AG fault are determined in accordance with Eq. (9). The results of the Pearson values for each IMF are shown in Fig. 12. It is evident that the dominating mode, IMF 2, has the largest Pearson coefficient (R2). A Teager Kaiser energy operator from is used to process the obtained dominating mode IMF2 to compute the energy $\psi(k)$. Ultimately, it serves as a signal for fault detection. An extensive simulations are carried out for both symmetrical and unsymmetrical faults on Fig. 6, the threshold (ε_T) for fault detection is chosen at 0.2.

Case 1: Performance on internal faults

Fig. 13 demonstrates the initiation of a three-phase fault at 0.55 seconds, located 100km prior to the STATCOM, with a fault inception angle of $10°$, a VRM of 0.97p.u, and a wind speed of 15 m/s. Fig. 14 illustrates the performance of fault detection during a three-phase fault, while Fig. 15 indicates that fault detection is achieved within just 5ms, with the fault detection unit result is 1.

Case 2: Performance on close in single-phase fault

To assess the effectiveness of the proposed fault detection technique, a single-phase fault is initiated at 0.5 seconds, 1km from R_G, with a fault resistance of 10Ω, a fault inception angle of $60°$, VRM mode (with V_{ref} set to 0.95p.u). and a wind speed is 15 m/s. Fig. 16 depicts the performance of fault detection during a single-phase fault, while Fig. 17 shows that fault detection was accomplished in just 9ms, with the fault detection unit registering a result of 1.

Case 3: Performance on non-fault events

To evaluate the proposed fault detection algorithm under non-fault conditions, inductive switching (60% sudden load change) and capacitor switching (40% of the total MVAR demand) are simulated at Bus-W. The system operates in VAR control mode with Q_{ref} set to -0.75p.u, and the wind speed is 10 m/s. Figs. 18 and 19 illustrate the fault detection performance during these inductive load and capacitor load switching scenarios. Fig. 20 clearly shows that for both inductive and capacitive load variations during non-fault transients, the fault detection unit remains at zero.

Case 4: Performance evaluation with noise in current signals

To evaluate the proposed fault detection algorithm during noisy current signals, a scenario with a signal-to-noise ratio (SNR) of 30 dB is analyzed. This involves a three-phase fault occurring at 260km after the STATCOM, with a fault inception angle of $45°$, fault resistance of 10Ω, and STATCOM operating in VARCM mode (with Q_{ref} at +0.75p.u). The wind speed is 10 m/s, as illustrated in Figs. 21 and 22. As shown in Figs. 21 and 22, the fault was detected within just 9ms, with a fault detection response unit of 1.

Case 5: Performance evaluation during current transformer (CT) saturation

During severe three-phase short circuit condition sometimes, the cores of protective CTs get saturated, which causes an inaccurate representation of the primary fault current. To evaluate the proposed fault detection algorithm, a three-phase fault is introduced 90km before the STATCOM, with a fault inception angle of $60°$, with R_f of 5Ω, mode of operation set to VRM (with V_{ref} at 1.03p.u) and a wind speed is 5 m/s, as depicted in Figs. 23 and 24. It is evident that the proposed fault detection algorithm performs effectively, identifying faults within 8ms. This highlights the robustness of the suggested protection method in handling CT saturation.

Case 6: Performance evaluation during double circuit line

To evaluate the performance of the proposed scheme under conditions of double circuit transmission line, single phase to ground fault is created at 0.5 sec at 320km with fault resistance of 10Ω, fault inception angle is 600, VRM mode (V_{ref} =0.95p.u), wind speed (v) is15m/s from grid side relay R_G of the double circuit line as shown in Fig. 25. Hence Fig. 26 and Fig. 27, indicates that the fault is detected within 5ms and fault detection unit is 1.

Case 7: Performance evaluation during source impedance change

a) High source impedance ratio (SIR is 7) effect on proposed fault detection algorithm

To evaluate the performance of the proposed scheme under conditions of high impedance source ratio, single phase to ground fault is created at 0.5 sec at 300km with fault resistance of 15Ω, fault inception angle is $140°$, VRM mode (V_{ref} =0.97p.u), wind speed (v) is 10m/s from grid side relay R_G. Fig. 28 and Fig.

Table 15. PSO-RVFLN classifier sample test results.

Type of fault	Location of fault in km	Resistance of fault in (Ω)	STATCOM modes	Wind speed (m/s)	Fault inception angle (°)	Fault classification time (T_1) (ms)	MJO-RVFLN classified as
AG		50	10	VRM	10	60	8	AG
ABG	Before STATCOM	100	5		5	45	6	ABG
AB		60	15		15	120	5	AB
ABC		120	10		10	180	6	ABC
AG		220	5		10	60	7	AG
ABG	After STATCOM	340	10	VARCM	10	90	9	ABG
AB		260	60		15	150	8	AB
ABC		360	100		10	180	6	ABC

Table 16. Percentage accuracy and confusion matrix of the suggested PSO-RVFLN classifier.

Fault type	1	2	3	4	5	6	7	8	9	10	Proposed MJO-RVFLN (%) classification accuracy
1	538					2					99.62
2		538					2				99.62
3			538					2			99.62
4				520			20		4		96.29
5					517			23			95.74
6						528			12		97.77
7	5	3		11			523				96.85
8		8	10		2			520			96.29
9			9			5			526		97.40
10		2								538	99.62
			Total average percentage accuracy								**97.88**

Table 17. Proposed RVFLN, PSO-RVFLN, and MJO-RVFLN accuracy in percentage.

Proposed algorithm	Percentageaccuracy
RVFLN	95.12
PSO-RVFLN	97.88
MJO-RVFLN	99.97

29 indicates that the proposed fault detection algorithm performs effectively, identifying faults within 8ms and fault detection unit is 1.

b) Medium source impedance ratio (SIR is 5) effect on proposed fault detection algorithm

To evaluate the performance of the proposed scheme under conditions of medium source Impedance ratio, single phase to ground fault is created at 0.5 sec at 320km with fault resistance of 10Ω, fault inception angle is $160°$, VRM mode (V_{ref} =0. 95p.u), wind speed (v) is 10m/s from grid side relay R_G. Fig. 30 and Fig. 31 indicates that the proposed fault detection algorithm performs effectively, identifying faults within 7ms and fault detection unit is 1.

c) Low source impedance ratio (SIR is 3) effect on proposed fault detection algorithm

To evaluate the performance of the proposed scheme under conditions of low source Impedance ratio, single phase to ground fault is created at 0.5 sec at 340km with fault resistance of 10Ω, fault inception angle is $120°$, VRM mode (V_{ref} =0. 98p.u), wind speed (v) is15m/s from grid side relay R_G. Fig. 32 and Fig. 33 indicates that the proposed fault detection algorithm performs effectively, identifying faults within 5ms and fault detection unit is 1.

Case 8: Performance evolution during uncertainties in the transmission lines parameters

Any uncertainties or variations in transmission line parameter due to factors like temperature changes, aging, or environmental condition can affect signal characteristics and small degrade fault detection performance. Fig. 34, and Fig. 35 shows that during variations in transmission line parameters like resistance and inductance the proposed fault detection algorithm performs effectively, identifying faults within 7ms and fault detection unit is 1. Fig. 34, it indicates that, the proposed method is does not affect due to parameter variations of the transmission line.

5.2. Results PSO-VMD-MJO-RVFLN fault classification algorithm

The performance of conventional phasor-based fault classification techniques may be impacted by the irregular current waveform pattern close to the wind farm. In order to solve this issue, the fault classification operation in this study is completed using the grid side's current signals. The suggested approach uses an PSO-VMD based MJO-RVFLN classifier to complete the fault classification task. To test the proposed classifier, a three phase fault is created at 150km before STATCOM with fault inception angle is $60°$, fault resistance is 10Ω,wind speed is 10m/s and VRM mode (V_{ref} is 1.02p.u) as show in Fig. 36. The results of PSO-VMD ,the optimal number of modes (K) is 5 and α is 1628, the obtained IMFs are shown in Fig. 37.

The features selection of proposed MJO-RVFLN classifier is as follows: As seen in Fig. 37. The IMF_1 experiences a notable change in magnitude during the fault. As show in Fig. 38. Q_1 and Q_3 are the first and third quartiles of the IMF_1 data. It clearly indicates the low interquartile range of the IMF_1. As can be seen in Fig. 38, there are a no outliers and the median is nearly at its maximum. The IMF_1 is a great feature for fault classification because of this characteristic. To generate the feature set, the current signal one cycle post-fault IMF_1 is computed, as indicated by Eq. (24).

$$X = \sum_{j-N}^{N} |IMF_{1j}| \tag{24}$$

The phase A energy (E_A) is determined as follows:

$$E_A = \sum_{p=1}^{n} [X]^2 \tag{25}$$

Similarly, Eq. (25) is used to compute the remaining energy E_B and E_C and ground energy E_Z.

Similarly, in all symmetrical and un symmetrical faults IMF_1 has taken as best feature to determine the feature data using Eq. (25). Fig. 39 shows that the sample feature data set for both symmetrical/unsymmetrical faults.

Matlab software was used to run extensive simulations that produced a dataset containing a variety of fault types, as shown in Fig. 1. The best feature was determined to be the first Intrinsic Mode Function (IMF_1), and Eq. (25), which yielded the appropriate energies (E_A, E_B, E_C, and E_Z), was used to compute them. Table 1 shows that 5,400 samples were set aside for testing, and a total of 16,800 samples were used for training. For testing reasons, 540 samples were chosen for each category of fault.

As shown in Fig. 8, the four feature energies are fed into the MJO-RVFLN model as inputs for fault classification. During this process, to train the model with 70% of the data and to test the model with 5,400 samples. The RVFL network's hyper parameters are, linear scale, scale modes, hidden neurons, bias, direct link, Radbas activation function. The search space is defined to identify the optimal set of hyper parameters that enhance the performance of the RVFL network, as illustrated in Table 3.

Using the defined search space for the RVFL network's hyperparameters optimization , the resulting configuration of the

Table 18. Comparison results of proposed protection scheme with existing methods in literature.

Ref.	Technique used	Sampling frequency (kHz)	Network consists of	Max R_f Ω	Fault detection/Classification time (ms)	Accuracy (%)		CT sat	Fault detection affected by		
						Fault detection unit	Fault classification unit		Inductive switching	Capacitive switching	Signal noise
[23]	Clark transform correlation coefficients	2.4	Wind farm	500	10	NM	NM	NM	NM	NM	No
[24]	New adaptive relaying	10	STATCOM	NC	20	100	NM	NM	No	No	No
[25]	DWT–spectral energy	2	STATCOM	100	NC	NM	NM	NM	No	No	NM
[28]	DFT adaptive relaying	1	STATCOM–wind farm	200	NC	100	NM	NM	No	No	No
[22]	Dual time transform (DT)	10	STATCOM–wind farm	100	8	100	99.96	No	No	No	No
[26]	Least square transient detection coefficient	1	DFIG–wind farm–STATCOM	100	8	100	100	NM	No	No	No
[27]	Differential current ration	1	STATCOM	200	10	100	NM	No	No	No	No
[7]	Transient energy and TT transform	1	DFIG–wind farm	100	10	100	100	No	No	No	No
Proposed method	PSO–VMD–DMF–TKEO, PSO–VMD–MJO–RVFLN	8	STATCOM–wind farm	100	10	100	99.97	No	No	No	No

RVFL network is obtined which is presented in Tables 5 and 6 respectively.

The training phase is applied to each optimal RVFLN configuration listed in Tables 5 and 6, and the Mean Squared Error (MSE) is computed using the following equation.

$$\textbf{Fitness} = \sum_{k=1}^{N} \frac{\sum_{i=1}^{m} \left(X - \hat{X} \right)^2}{N} \tag{26}$$

where $\hat{X}$ is the desired output, X is the actual output, N is the number of training samples, and m is the number of outputs. The optimal RVFLN setup is then identified.

5.3. Test results for the classifier method based on MJO-RVFLN with fault location both before and after STATCOM

Classification Accuracy (CA) is defined as the ratio of correctly identified faults to the total number of faults, and it is expressed by Eq. (27).

$$CA = \frac{\textbf{Correctly identified faults}}{\textbf{Total number of faults}} X100\% \tag{27}$$

According to Table 7, the suggested MJO-RVFLN method's fault classification time, expressed in milliseconds (ms) for the tested fault situation, is less than half a cycle.

A) Test results for the classifier method based on MJO-RVFLN with fault location both before and after STATCOM during noise condition

To validate the efficacy of the proposed methods, the different noisy test data sets with the SNR of 20, 30, and 40 dB is considered. A few test outcomes are listed in Tables 9, 11 and 13 representing the proposed method performance under a distinct noisy environment. The Tables 10, 12, and 14 result proves the robustness of the proposed method with noise variations.

5.4. Test results for the classifier method based on PSO-RVFLN with fault location both before and after STATCOM

Eq. (27) is used to compute the accuracy of the classifier. Table 15 indicates that the fault classification time for the proposed PSO-RVFLN method, measured in milliseconds (ms) for the fault case being tested, is under half a cycle.

Fig. 41, demonstrates that the proposed MJO-RVFLN classifier outperformed the PSO-RVFLN classifier in terms of metrics like Recall, Precision, and F1-Score on the testing dataset.

6. COMPARISON WITH OTHER REPORTED WORKS IN LITERATURE

The proposed fault detection relaying scheme is validated with different internal faults, non-fault events, noise condition and CT saturation cases. On other hand the proposed classifier is validated with faults before and after STATCOM. Table 18 demonstrates that the proposed methods achieved a 100% success rate in fault detection and a 99.97% accuracy in fault classification, effectively protecting the STATCOM-compensated transmission line integrated with DFIG.The time required for proposed relaying algorithm is within half a cycle.

7. CONCLUSIONS

This paper introduces a new relaying algorithm that utilizes for transmission lines that link the DFIG wind farms with STATCOM compensation. Combining Particle Swarm Optimization (PSO) with Variational Mode Decomposition (VMD), Dominant Mode Filtering (DMF), and the Teager-Kaiser Energy Operator (TKEO) creates an effective method for fault detection and it attains 100% fault detection accuracy. The Modified Jellyfish Optimization (MJO) algorithm with the Random Vector Functional Link Network (RVFLN) classifier provides an improved approach to fault classification. The MJO algorithm enhances the RVFLN classifier by optimizing its hyper parameters, resulting in greater learning efficiency and achieved a classification accuracy of 99.97%. Moreover, the proposed relaying algorithm detects and classifies faults within half a cycle, thereby enhancing system reliability. Furthermore, the suggested approach uses fewer inputs, which reduces the computational burden and achieved the performance metrics like Precision (0.995), Recall (0.992) and F1-Score (0.994).

7.1. Limitations

The PSO-VMD, DMF, and TKEO require significant processing power, making real-time implementation challenging. The MJO for RVFL network tuning requires time consuming and DMF and TKEO face difficulty with highly distorted signals. Finally, the DFIG-STATCOM fluctuations can interfere with fault signatures, requiring adaptive thresholding which is critical in realistic scenario.

7.2. Future scope

- In this manuscript, relaying methods are developed to protect transmission line linked to DFIG-based type-3 WTGs. Permanent magnet synchronous generator (PMSG)-based type-4 WTGs are now considered to be more beneficial have enhanced fault response capabilities and are integrated into the grid. Therefore, in order to possibly build a new solution, it is required to examine the effects of incorporating these type-4 WTGs into the distance relaying scheme.
- The future research work may be extended to develop threshold free adaptive relaying algorithms for protecting STATCOM compensated transmission line. The various deep learning algorithms such as convolutional neural network, recurrent neural network, long short time memory etc. can be used for classification of faults in such transmission line.

Appendix–A. Parameters and ratings of the power system equipment (DFIG-based system)

Power system equipment	Parameters of the equipment	Rating of parameters
DFIG wind farm	Wind farm rating	401.5 MW each
	Terminal voltage (kV)	0.575
	Frequency (Hz)	50
	Inertia constant (p.u)	1.3
	Resistance of the stator (p.u)	0.174
	Reactance of the stator (p.u)	0.172
	Resistance of the rotor (p.u)	0.013
	Reactance of the rotor (p.u)	0.242
	Resistance of the crowbar (p.u)	0.0428
Power converters	Power rating (kW)	280
	Switching frequency (kHz)	2.5
	Voltage of DC link (V)	1030
	Capacitance of DC link (μF)	10500
LCL filter	Inductance of grid side (p.u)	0.016
	Capacitance of the filter (p.u)	0.103
	Inductance of converter side (p.u)	0.678
Transformer–1	Rating	575 V / 25 kV
	Capacity	1.70 MVA
Transformer–2	Rating	25 kV / 400 kV
	Capacity	100 MVA
Collector line	Total length	10km
	Z_1 impedance (Ω/km)	0.114 + j0.32
	Z_0 impedance (Ω/km)	0.30 + j1.06
Transmission line	Total length	400km
	Z_1 impedance (Ω/km)	0.1321 + j0.321
	Z_0 impedance (Ω/km)	0.3451 + j1.301
	Positive and zero sequence capacitance (Ω/km)	0.013e–6, 0.005e–6
STATCOM	STATCOM rating	48-pulse, GTO, +/-100 MVAr, 400 kV
	DC side capacitor	2800 μF
	Coupling transformer	Four Δ/Y, 100 MVA, 400/15 kV Phase shift **7.5°**

REFERENCES

[1] *Wind Energy Engineering: A Handbook for Onshore and Offshore Wind Turbines*. Elsevier, 2 ed., 2023. 2nd Edition, May 8, 2023.

[2] F. Blaabjerg, Y. Yang, K. A. Kim, and J. Rodriguez, "Power electronics technology for large-scale renewable energy generation," *Proc. IEEE*, vol. 111, no. 4, pp. 335–355, 2023.

[3] N. Danapour, M. Tarafdar Hagh, and S. H. Hosseini, "Integrated wind turbines and power transmission line: A novel concept," *Sustain. Energy Technol. Assess.*, vol. 52, p. 102183, 2022.

[4] Z. Rafiee, R. Heydari, M. Rafiee, M. R. Aghamohammadi, and F. Blaabjerg, "Enhancement of the lvrt capability for dfig-based wind farms based on short-circuit capacity," *IEEE Syst. J.*, vol. 16, no. 2, pp. 3237–3248, 2022.

[5] S. Kamel, B. Mansour, and B. Faouzi, "Enhancement of dfig operation using a statcom under a voltage grid faults," in *Proc. 8th Int. Conf. Control, Decis. Inf. Technol. (CoDIT)*, (Istanbul, Turkey), pp. 1550–1555, 2022.

[6] Y. Chen, M. Wen, X. Yin, Y. Cai, and J. Zheng, "Distance protection for transmission lines of dfig-based wind power integration system," *Int. J. Electr. Power Energy Syst.*, vol. 100, pp. 438–448, 2018.

[7] B. Anudeep, P. K. Nayak, and S. Biswas, "An improved protection scheme for dfig-based wind farm collector lines," *Electr. Power Syst. Res.*, vol. 211, p. 108224, 2022.

[8] N. Rezaei, M. N. Uddin, I. K. Amin, M. L. Othman, M. B. Marsadek, and M. M. Hasan, "A novel hybrid machine learning classifier-based digital differential protection scheme for intertie zone of large-scale centralized dfig-based wind farms," *IEEE Trans. Ind. Appl.*, vol. 56, no. 4, pp. 3453–3465, 2020.

[9] M. N. Uddin, N. Rezaei, and M. S. Arifin, "Hybrid machine learning-based intelligent distance protection and control schemes with fault and zonal classification capabilities for grid-connected wind farms," *IEEE Trans. Ind. Appl.*, vol. 59, no. 6, pp. 7328–7340, 2023.

[10] O. D. Naidu, N. George, and V. Pradhan, "Distance protection for lines connected with type iii wind farms: Problems and solution," in *Proc. IEEE PES 15th Asia-Pacific Power and Energy Eng. Conf. (APPEEC)*, pp. 1–6, 2023.

[11] J. Barati, S. G. Seifossadat, and M. Joorabian, "A new adaptive coordination scheme of distance relays in dfig-based wind farm collector lines and transmission line compensated by statcom," *Int. Trans. Electr. Energy Syst.*, vol. 31, p. e13205, 2021.

[12] U. Karaagac, I. Kocar, J. Mahseredjian, L. Cai, and Z. Javid, "Statcom integration into a dfig-based wind park for reactive power compensation and its impact on wind park high voltage ride-through capability," *Electr. Power Syst. Res.*, vol. 199, p. 107368, 2021.

[13] K. Jia, Z. Yang, L. Zheng, Z. Zhu, and T. Bi, "Spearman correlation-based pilot protection for transmission line connected to pmsgs and dfigs," *IEEE Trans. Ind. Inf.*, vol. 17, no. 6, pp. 4532–4544, 2021.

[14] J. Ma, W. Zhang, J. Liu, and J. S. Thorp, "A novel adaptive distance protection scheme for dfig wind farm collector lines," *Int. J. Electr. Power Energy Syst.*, vol. 94, pp. 234–244, 2018.

[15] P. Mundra, A. Arya, S. K. Gawre, S. Biswal, F. V. Lopes, and O. P. Malik, "Taylor series based protection starting element for statcom compensated transmission line," *Electr. Power Syst. Res.*, vol. 204, p. 107700, 2022.

[16] J. Zare and S. P. Azad, "A new relaying scheme for protection of transmission lines connected to dfig-based wind farms," *IET Renew. Power Gener.*, vol. 15, pp. 2971–2982, 2021.

[17] X. Li, Y. Lu, T. Huang, J. Qin, and W. Jiang, "Superimposed components-based distance protection of lines emanating from dfig-based wind farms," *Electr. Power Syst. Res.*, vol. 208, p. 107916, 2022.

[18] M. M. Mobashsher, A. A. Abdoos, S. M. Hosseini, S. M. Hashemi, and M. Sanaye-Pasand, "An accelerated distance protection scheme for the lines connected to inverter-based resources," *IEEE Syst. J.*, vol. 17, no. 4, pp. 6272–6281, 2023.

[19] A. Saber, M. F. Shaaban, and H. H. Zeineldin, "A new differential protection algorithm for transmission lines connected to large-scale wind farms," *Int. J. Electr. Power Energy Syst.*, vol. 141, p. 108220, 2022.

[20] X. Zhang, M. Radwan, and S. P. Azad, "Modified distance protection of transmission lines originating from dfig-based wpps by considering the impact of fault-induced rotor frequency and lvrt requirements," *Int. J. Electr. Power Energy Syst.*, vol. 147, p. 108911, 2023.

[21] J. d. J. Chavez, M. Popov, D. López, V. Terzija, and S. Azizi, "Robust distance protection for cross-country faults in power grids with high penetration of inverter-based resources," *e-Prime Adv. Electr. Eng. Electron. Energy*, vol. 9, p. 100708, 2024.

[22] S. Biswas, P. K. Nayak, and G. Pradhan, "A dual-time transform assisted intelligent relaying scheme for the statcom-compensated transmission line connecting wind farm," *IEEE Syst. J.*, vol. 16, pp. 2160–2171, 2022.

[23] X. Chen, X. Yin, and Z. Zhang, "Impacts of dfig-based wind farm integration on its tie line distance protection and countermeasures," *IEEE Trans. Electr. Electron. Eng.*, vol. 12, no. 4, pp. 553–564, 2017.

[24] A. R. Singh, N. R. Patne, and V. S. Kale, "Synchronized measurement based an adaptive distance relaying scheme for statcom compensated transmission line," *Measurement*, vol. 116, pp. 96–105, 2018.

[25] S. K. Mishra, L. N. Tripathy, and S. C. Swain, "Dwt approach based differential relaying scheme for single circuit and double circuit transmission line protection including statcom," *Ain Shams Eng. J.*, vol. 10, pp. 93–102, 2019.

[26] S. Biswas and B. K. Panigrahi, "An improved fault detection and phase identification for collector system of dfig-wind farms using least square transient detector coefficient," *Electr. Power Syst. Res.*, vol. 226, p. 109961, 2024.

[27] S. Gangolu, S. Sarangi, and R. Mohanty, "Relay algorithm for statcom compensated line using differential current ratio," *Int. J. Electr. Power Energy Syst.*, vol. 155, p. 109473, 2024.

[28] S. Biswas and P. K. Nayak, "A new approach for protecting tcsc compensated transmission lines connected to dfig-based wind farm," *IEEE Trans. Ind. Inf.*, vol. 17, pp. 5282–5291, 2021.

[29] S. K. Mohanty, P. K. Nayak, P. K. Bera, and H. H. Alhelou, "An enhanced protective relaying scheme for tcsc compensated line connecting dfig-based wind farm," *IEEE Trans. Ind. Inf.*, vol. 20, pp. 3425–3435, 2024.

[30] S. Mishra, S. Gupta, and A. Yadav, "Teager energy assisted variational mode decomposition-based fault location technique for statcom compensated system," *Int. J. Numer. Model. Electron. Netw. Devices Fields*, vol. 36, p. e3093, 2023.

[31] O. Koduri, R. Ramachandran, and M. Saiveerraju, "A new relaying approach for protecting tcsc compensated transmission line connected to dfig based wind farm," *e-Prime Adv. Electr. Eng. Electron. Energy*, vol. 9, p. 100668, 2024.

[32] V. K. Peddiny, B. Datta, and A. Banerjee, "Performance improvement of combined wind farms using ann-based statcom and grey wolf optimization-based tuning," *J. Oper. Autom. Power Eng.*, vol. 13, no. 3, pp. 248–254, 2025.

[33] P. Niranjan, N. K. Choudhary, N. Singh, and R. K. Singh, "Optimal coordination of dual-setting directional over current relay in microgrid considering multi-parametric characteristics," *J. Oper. Autom. Power Eng.*, vol. 13, no. 2, pp. 174–183, 2025.

[34] P. Venkata, V. Pandya, and A. Sant, "Data mining and svm based fault diagnostic analysis in modern power system using time and frequency series parameters calculated from full-cycle moving window," *J. Oper. Autom. Power Eng.*, vol. 12, no. 3, pp. 206–214, 2024.

[35] N. K. Sharma, S. R. Samantaray, and C. N. Bhende, "Vmd-enabled current-based fast fault detection scheme for dc microgrid," *IEEE Syst. J.*, vol. 16, pp. 933–944, 2022.

[36] X. B. Wang, Z. X. Yang, and X. A. Yan, "Novel particle swarm optimization-based variational mode decomposition method for the fault diagnosis of complex rotating machinery," *IEEE/ASME Trans. Mechatron.*, vol. 23, pp. 68–79, 2018.

[37] X. Chen, Y. Yang, Z. Cui, and J. Shen, "Vibration fault diagnosis of wind turbines based on variational mode decomposition and energy entropy," *Energy*, vol. 174, pp. 1100–1109, 2019.

[38] T. M. Shami, A. A. El-Saleh, M. Alswaitti, Q. Al-Tashi, M. A. Summakieh, and S. Mirjalili, "Particle swarm optimization: A comprehensive survey," *IEEE Access*, vol. 10, pp. 10031–10061, 2022.

[39] P. D. Raval and A. S. Pandya, "A hybrid pso-ann-based fault classification system for ehv transmission lines," *IETE J. Res.*, vol. 68, pp. 3086–3099, 2022.

[40] A. K. Malik, R. Gao, M. A. Ganaie, M. Tanveer, and P. N. Suganthan, "Random vector functional link network: Recent developments, applications, and future directions," *Appl. Soft Comput.*, vol. 143, p. 110377, 2023.

[41] J.-S. Chou and D.-N. Truong, "A novel metaheuristic optimizer inspired by behavior of jellyfish in ocean," *Appl. Math. Comput.*, vol. 389, p. 125535, 2021.

[42] G. Yildizdan, "Mjs: a modified artificial jellyfish search algorithm for continuous optimization problems," *Neural Comput. Appl.*, vol. 35, pp. 3483–3519, 2023.

[43] M. Abdel-Basset, R. Mohamed, R. K. Chakrabortty, M. J. Ryan, and A. El-Fergany, "An improved artificial jellyfish search optimizer for parameter identification of photovoltaic models," *Energies*, vol. 14, p. 1867, 2021.